NeuroImage: Clinical 34 (2022) 102989

Contents lists available at ScienceDirect

NeuroImage: Clinical

journal homepage: www.elsevier.com/locate/ynicl

Diagnostic accuracy of quantitative susceptibility mapping in multiple system atrophy: The impact of echo time and the potential of histogram analysis

Marta Lancione [a,b], Matteo Cencini [a,b], Mauro Costagli [a,c,*], Graziella Donatelli [b,d], Michela Tosetti [a,b], Giulia Giannini [e,f], Roberta Zangaglia [g], Giovanna Calandra-Buonaura [e,f], Claudio Pacchetti [g], Pietro Cortelli [e,f], Mirco Cosottini [d]

[a] IRCCS Stella Maris, Pisa, Italy
[b] IMAGO7 Foundation, Pisa, Italy
[c] Department of Neuroscience, Rehabilitation, Ophthalmology, Genetics, Maternal and Child Sciences (DINOGMI), University of Genova, Genova, Italy
[d] Azienda Ospedaliero-Universitaria Pisana, Pisa, Italy
[e] Dipartimento di Scienze Biomediche e Neuromotorie, Università di Bologna, Bologna, Italy
[f] IRCCS Istituto delle Scienze Neurologiche di Bologna, Bologna, Italy
[g] Parkinson and Movement Disorder Unit, IRCCS Mondino Foundation, Pavia, Italy

ARTICLE INFO

Keywords:
Quantitative susceptibility mapping
Echo-time-dependent QSM
Multiple system atrophy
QSM optimization
QSM diagnostic accuracy
Histogram analysis

ABSTRACT

The non-invasive quantification of iron stores via Quantitative Susceptibility Mapping (QSM) could play an important role in the diagnosis and the differential diagnosis of atypical Parkinsonisms. However, the susceptibility (χ) values measured via QSM depend on echo time (TE). This effect relates to the microstructural organization within the voxel, whose composition can be altered by the disease. Moreover, pathological iron deposition in a brain area may not be spatially uniform, and conventional Region of Interest (ROI)-based analysis may fail in detecting alterations. Therefore, in this work we evaluated the impact of echo time on the diagnostic accuracy of QSM on a population of patients with Multiple System Atrophy (MSA) of either Parkinsonian (MSAp) or cerebellar (MSAc) phenotypes. In addition, we tested the potential of histogram analysis to improve QSM classification accuracy.

We enrolled 32 patients (19 MSAp and 13 MSAc) and 16 healthy controls, who underwent a 7T MRI session including a gradient-recalled multi-echo sequence for χ mapping. Nine histogram features were extracted from the χ maps computed for each TE in atlas-based ROIs covering deep brain nuclei, and compared among groups.

Alterations of susceptibility distribution were found in the Putamen, Substantia Nigra, Globus Pallidus and Caudate Nucleus for MSAp and in the Substantia Nigra and Dentate Nucleus for MSAc. Increased iron deposition was observed in a larger number of ROIs for the two shortest TEs and the standard deviation, the 75th and the 90th percentile were the most informative features yielding excellent diagnostic accuracy with area under the ROC curve > 0.9.

In conclusion, short TEs may enhance QSM diagnostic performances, as they can capture variations in rapidly-decaying contributions of high χ sources. The analysis of histogram features allowed to reveal fine heterogeneities in the spatial distribution of susceptibility alteration, otherwise undetected by a simple evaluation of ROI χ mean values.

1. Introduction

Multiple System Atrophy (MSA) is a rare neurodegenerative disorder characterized by a combination of autonomic dysfunctions (cardiovascular autonomic failure and urogenital dysfunctions) plus cerebellar syndrome and/or Parkinsonism. The current diagnostic criteria define three degrees of certainty for diagnosis (possible, probable and definite) and two phenotypes, Parkinsonian (MSAp) or

* Corresponding author at: Viale del Tirreno, 331 - 56128 Pisa, Italy.
E-mail address: mauro.costagli@fsm.unipi.it (M. Costagli).

https://doi.org/10.1016/j.nicl.2022.102989
Received 28 December 2021; Received in revised form 25 February 2022; Accepted 10 March 2022
Available online 11 March 2022

cerebellar (MSAc), according to the predominant features at the time of evaluation (Gilman et al., 2008). Even though it is still a matter of debate whether iron accumulation is a cause or a consequence of the neurodegenerative process (Berg and Hochstrasser, 2006), increased iron deposition has been documented in many deep gray matter nuclei of MSA patients. Histopathological studies, indeed, reported iron deposition in the posterolateral putamen (Dickson et al., 1999), in substantia nigra pars compacta, globus pallidus (Jellinger, 2003), caudate nucleus (Dexter et al., 1991) and dentate nucleus (Matsusue et al., 2009).

Iron store could represent an important biomarker for the diagnosis and the differential diagnosis of neurodegenerative diseases and Quantitative Susceptibility Mapping (QSM) is a powerful tool for its non-invasive and quantitative assessment in vivo via Magnetic Resonance Imaging (MRI) (de Rochefort et al., 2010; Deistung et al., 2016; Haacke et al., 2015; Liu et al., 2015; Reichenbach et al., 2015; Shmueli et al., 2009; Wang and Liu, 2015). QSM derives the magnetic susceptibility of the tissues, which correlates with iron concentration (Langkammer et al., 2012), from the phase of a T2*-weighted Gradient Recalled Echo (GRE) signal. The provided information is quantitative and spatially specific, as the non-local distortions induced by susceptibility sources on the magnitude of T2*-weighted signals are removed. For these reasons, QSM is gaining increasing importance in the study of neurodegenerative disorders (Düzel et al., 2021; Ravanfar et al., 2021), including Parkinson's disease (Acosta-Cabronero et al., 2017; Guan et al., 2019; Langkammer et al., 2016; Lotfipour et al., 2012) and atypical Parkinsonisms (Azuma et al., 2019; Wang et al., 2019). Concerning MSA, previous studies reported altered susceptibility in putamina, substantia nigra, red nuclei, subthalamic nuclei and, for MSAc, in dentate nuclei (Ito et al., 2017; Mazzucchi et al., 2019; Sjöström et al., 2017; Sugiyama et al., 2019), yielding good diagnostic accuracy in discriminating MSA patients to both healthy controls and other Parkinsonisms.

Recent works reported that measured susceptibility values depend on several experimental factors. First of all, susceptibility anisotropy impairs QSM accuracy in white matter, where the highly organized microstructure of myelin sheath introduces a dependence of measured susceptibility on the orientation of fibers with respect to the external magnetic field (Lancione et al., 2017; Li et al., 2012; Liu et al., 2011; Wharton and Bowtell, 2015). In addition, the dependence of QSM on acquisition parameters such as coverage (Elkady et al., 2016; Karsa et al., 2018), spatial resolution (Karsa et al., 2018; Zhou et al., 2017) and Echo Time (TE) (Biondetti et al., 2020; Cronin et al., 2017; Lancione et al., 2019; Sood et al., 2017) was demonstrated. The dependence on TE is due to the non-linear time-evolution of the phase signal, possibly reflecting the presence of multiple signal components caused by sub-voxel compartmentalization and microstructures (Sati et al., 2013; Sood et al., 2017; Wharton and Bowtell, 2012; Xu et al., 2018). A previous study at 3T reported that it can yield variations of QSM values in intact tissues up to approximately 100 parts per billions (ppb) and beyond 1000 ppb for cerebral microbleeds (Cronin et al., 2017). On these premises, as pathological processes can affect sub-voxel composition, we hypothesize that χ maps computed at different TEs may provide different and complementary diagnostic information. An assessment of the influence of TE on the diagnostic accuracy of QSM is currently missing.

The vast majority of QSM studies targeting the deep gray matter nuclei are based on the measurement of mean susceptibility in manually-drawn or automatically-selected regions of interest (ROI). However, the iron deposition in nuclei affected by the disease might not be uniform, as also reported by histological studies (e.g. in MSA the putamen is mainly involved in its posterolateral portion (Dickson et al., 1999)). In these cases, the mean value would provide a partial and inaccurate estimate of iron distribution. Histogram analysis performed on the whole nucleus may provide a more comprehensive overview of the susceptibility distribution and the underlying iron deposition pattern, reflecting its spatial heterogeneity (Zhang et al., 2022).

The goal of the present study was twofold. First, we aimed to assess the impact of TE-dependency of QSM on the accuracy of differential diagnosis in a cohort of MSA patients of both Parkinsonian and cerebellar variants and a population of healthy controls. Second, we explored the potential of histogram analysis in enhancing the diagnostic performance of QSM. To these purposes, we enrolled a cohort of patients with MSA and a population of healthy controls and acquired multi-echo GRE data on a 7T MRI system. We reconstructed a susceptibility map for each TE of the multi-echo GRE sequence separately and performed histogram analysis on a set of ROIs selected from published atlases covering ten deep gray matter nuclei.

2. Methods

2.1. Study group

We enrolled patients with a diagnosis of possible or probable MSA referring to the Movement Disorders and Autonomic Disorders centers of the University of Bologna, Italy, and to the Parkinson and Movement Disorder Unit of IRCCS Mondino Foundation in Pavia, Italy during 2019–2020. Diagnosis of MSA was independently confirmed by three movement disorder specialized neurologists (PC, GCB, CP) according to current consensus criteria (Gilman et al., 2008). The MSA phenotype was defined as MSAp or MSAc on the basis of the predominant motor involvement at the time of the last clinical evaluation. The absence of non-supporting features for MSA were mandatory for inclusion in the study. Disease duration was defined as the time interval between the onset of the first MSA-related symptom and enrollment in this study.

We recruited 32 patients with MSA: 19 MSAp (11 females, 65 $\pm$ 8 [51–76] years old, 4 possible and 15 probable MSAp, disease duration = 5.3 $\pm$ 2.2 [3–9] years) and 13 MSAc patients (5 females, 60 $\pm$ 7 [48–72] years old, all probable MSAc, disease duration = 6.0 $\pm$ 3.0 [3–13] years). In addition, a population of 16 healthy controls (HC) and comparable age and sex distribution (6 females, 60 $\pm$ 10 [43–76] years old) was enrolled. The study was performed in accordance with the Declaration of Helsinki and approved by the Independent Ethics Committee of the local health service of Bologna (CE number: 18056, 212/2018/OSS/AUSLBO) and of Pavia (CE number: p-20180049076); all participants gave their written informed consent.

2.2. MRI acquisition hardware

All subjects underwent an ultra-high field MRI examination at the IMAGO7 Foundation in Pisa, Italy, using a GE Healthcare Discovery MR950 7T MRI system (GE Healthcare, Milwaukee, WI, USA). The patients were scanned within one month from the clinical evaluation. The scanner was equipped with a two-channel transmitter/32-channel receiver head coil (Nova Medical, Wilmington, MA, USA) and a gradient system with maximum amplitude = 50 mT/m and slew rate = 200 T/m/s.

2.3. MRI imaging protocol

The MRI protocol included a 3D Gradient Recalled Multi-Echo sequence (Susceptibility Weighted Angiography – SWAN, GE Healthcare) for the quantitative assessment of iron deposition. The sequence was prescribed axially with whole-brain coverage. The acquisition parameters were set as follows: TR = 54.1 ms; four equally spaced echoes: TE = 7.38, 16.36, 25.34, 34.32 ms; FA = 15°; in-plane FOV = 173 × 173 mm^2; axial coverage = 165.6 mm; acquired matrix size = 432 × 288 × 138; reconstructed voxel size = 0.6 × 0.6 × 1.2 mm^3; parallel imaging ASSET (Array Coil Spatial Sensitivity Encoding) acceleration factor = 2. Both the real and imaginary parts of the images obtained at each echo were saved and converted into magnitude and phase data.

2.4. Qualitative data inspection

The T2*-weighted images obtained from the magnitude of the 3D GRE signal were evaluated by a neuroradiologist and graded based on the severity of motion artifacts into three categories: "none/mild" corresponding to non-visible or little motion artifact, "moderate" for detectable motion and "severe" for extreme motion artifacts. Images affected by "severe" motion artifacts were excluded from the analysis.

2.5. Data processing

Susceptibility maps were computed via the following procedure. The raw phase images of individual echoes were unwrapped using a Laplacian-based algorithm (Li et al., 2012; Schofield and Zhu, 2003). A brain mask was generated using Brain Extraction Toolbox (bet) (Smith, 2002) in FSL 5.0.9 (FMRIB Software Library, Oxford Centre for Functional MRI of the Brain, Oxford, UK) on the T2*-weighted magnitude image averaged across echoes and then used for the removal of the background field via V-SHARP (Schweser et al., 2011). QSM images were obtained by applying the iLSQR (Li et al., 2015; Li et al., 2011) method separately to each individual echo. We used Laplacian-based phase unwrapping, V-SHARP and iLSQR implementations from STI Suite (MATLAB toolbox, available at https://people.eecs.berkeley.edu/~chunlei.liu/software.html from UC Berkeley, Berkeley, CA, USA). The susceptibility maps were visually inspected to ensure adequate image quality.

A study-specific template was also created using skull-stripped T2*-weighted magnitude images averaged across TEs of all subjects with Greedy-SyN approach and cross-correlation similarity metric (Avants et al., 2008) setting the parameters of antsMultivariateTemplateConstruction2 as follows: six template-construction iterations, 0.1 gradient step size, maximum $1000 \times 500 \times 250 \times 100$ multi-resolution iterations per registration, shrink factors $12 \times 8 \times 4 \times 2$, smoothing factors $4 \times 3 \times 2 \times 1$. The susceptibility maps of each echo were warped to the template space by applying the corresponding transformation. Then, they were averaged to create a study-specific QSM template.

2.6. QSM ROI-based analysis

Regions of interest were selected from the PD25 atlas (Xiao et al., 2017), from the probabilistic CIT168 atlas (Pauli et al., 2018) and from the probabilistic DN atlas (He et al., 2017). The selected ROIs were the following, each divided into left (L) and right (R) regions: Red Nucleus (RN), Subthalamic Nucleus (STN), Caudate Nucleus (CN), Putamen (Pu), Globus Pallidus externus (GPe) and internus (GPi), Thalamus (Th) from the PD25 atlas, Substantia Nigra pars compacta (SNc) and reticulata (SNr) from probabilistic CIT168 atlas, and Dentate Nucleus (DN) from DN atlas. Probabilistic ROIs were converted to binary masks by choosing a threshold of 0.5, in order to cover the whole anatomical regions without exceeding their borders and ensuring no overlap between SNr and SNc. The T2*-weighted template was non-linearly warped to the T2*-weighted version of the multi-contrast PD25 atlas via antsRegistration using cross-correlation similarity metric and nearest neighbor interpolation. By applying the inverse transformation, the ROIs from the PD25 atlas were warped to the study-specific template. To improve registration accuracy, the CIT168 atlas and DN atlas were warped from the MNI to the T1-weighted version of PD25 atlas and then to the study-specific template, after concatenating the two transforms in order to perform them in a single step.

For each ROI and for each subject in the study-specific template space we extracted the following histogram features for each TE: mean value, standard deviation, $10^{th}/25^{th}/50^{th}/75^{th}/90^{th}$ percentile, kurtosis and skewness. These are all the histogram features commonly examined in histogram analysis (Fujima et al., 2019, 2015; Zhang et al., 2022), except for the maximum and the minimum value which are extremely sensitive to noise and outliers. The histogram features were computed using the corresponding built-in function in MATLAB which employed the whole sample, making the calculation independent of histogram binning operations. QSM values were not referenced to any specific region (Acosta-Cabronero et al., 2016) to avoid assumptions on brain areas spared by MSA and were age- and sex-adjusted via linear regression (Thomas et al., 2021). Susceptibility measures were then expressed in parts per million (ppm).

2.7. Statistical analysis

Statistical analysis was performed in MATLAB (MathWorks, Natick, MA, USA). Sex distributions of the three populations (MSAc, MSAp and HC) were compared pair-wise via chi-square test, while age comparisons were carried out using Kruskall-Wallis omnibus test and post-hoc Dunn's test. The threshold of statistical significance was set to $p < 0.05$ after Dunn-Sidak correction for multiple comparisons. Non-parametric statistical tests were employed to analyze QSM data: the feature values among the three groups were compared with Kruskal-Wallis omnibus test, followed by Dunn's test and Dunn-Sidak correction for post-hoc analysis. Diagnostic accuracy was evaluated via the Area Under the Curve (AUC) of the Receiver Operating Characteristic (ROC) curve.

3. Results

After visual inspection and rating of the T2*-weighted magnitude images by a neuroradiologist, four subjects (1 MSAp, 3 MSAc) were excluded from QSM analysis due to severe motion artifacts. The remaining population of patients was demographically distributed as follows: 18 MSAp (10 females, 65 ± 8 [51–76] years old, disease duration $= 5.4 \pm 2.1$ [3–9] years, 4 possible and 14 probable MSAp) and 10 MSAc patients (4 females, 60 ± 7 [52–72] years old, disease duration $= 5.8 \pm 3.1$ [3–13] years, all probable MSAc). Other clinical features of MSA patients are reported in Supplementary Table S1. The susceptibility maps obtained for each TE are reported in Fig. 1 for two exemplary subjects.

No statistically significant differences between the distribution of the demographic features of sex and age were reported between healthy controls, MSAc and MSAp patients.

Nine histogram features (mean, standard deviation, $10^{th}/25^{th}/50^{th}/75^{th}/90^{th}$ percentile, kurtosis and skewness) were computed for each subject, TE and ROI. These covered ten nuclei divided into left and right sides which are displayed in Fig. 2 overlaid onto the study-specific template.

We compared the distribution of the histogram features between the MSAc and MSAp patients and healthy controls for each ROI and each TE. The obtained p-values are reported in Fig. 3. Statistical significance was reached for several ROIs and features, e.g., for the mean, the 75^{th} percentile, and above all for the standard deviation and the 90^{th} percentile computed at the first (TE01) and the second TE (TE02), respectively, for which up to fourteen ROIs reported significant difference among groups. These findings indicate a distributed pattern of pathological iron deposition. The tests performed at shortest TEs (i.e., TE01 and TE02) yielded higher levels of statistical significance, detecting group differences that were not observed with longer TEs.

In Fig. 4, we reported the mean susceptibility values computed at TE01 in all the ROIs for all subjects, divided into the three groups. In the post-hoc analysis, MSAp patients showed higher susceptibility in Pu bilaterally with respect to MSAc and HC, and higher susceptibility in GPi and GPe bilaterally with respect to HC. Increased iron deposition was also reported in left SNc for both phenotypes with respect to HC and higher susceptibility was observed in DN bilaterally for MSAc with respect to MSAp. The 90^{th} percentile and the standard deviation detected significant susceptibility differences between groups also in other ROIs, such as CN, SNr and right SNc (Supplementary Figs. S1 and S2). However, when the same features were extracted from

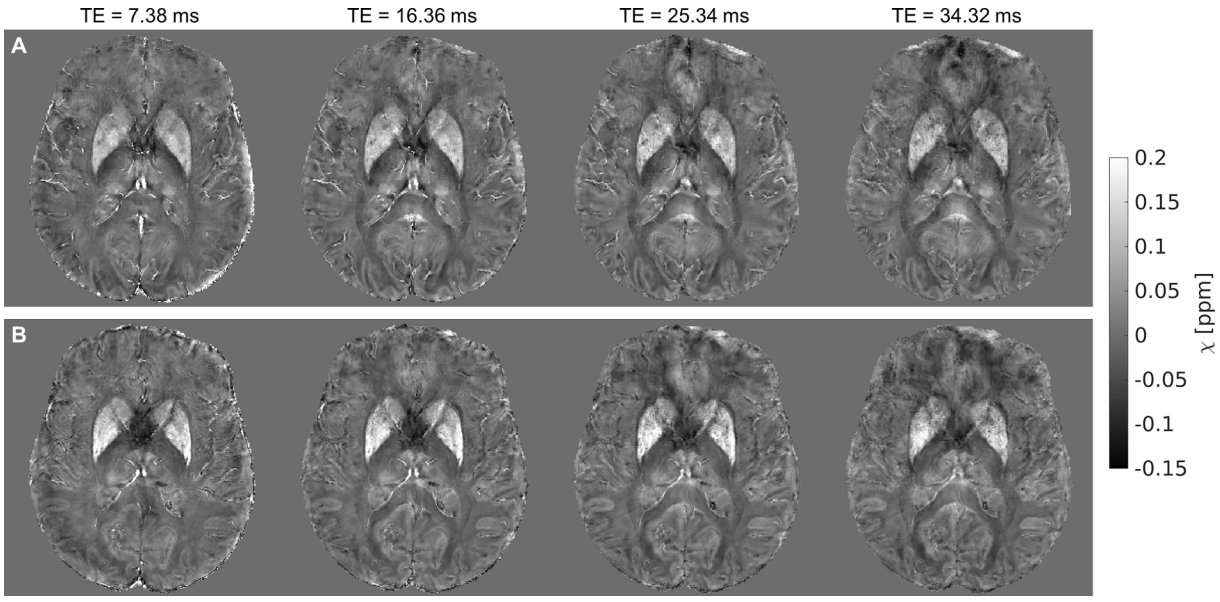

Fig. 1. Susceptibility maps computed for each TE for two representative subjects. Panel A shows a control subject with "none/mild" motion artifacts while panel B shows a patient with "moderate" motion artifacts.

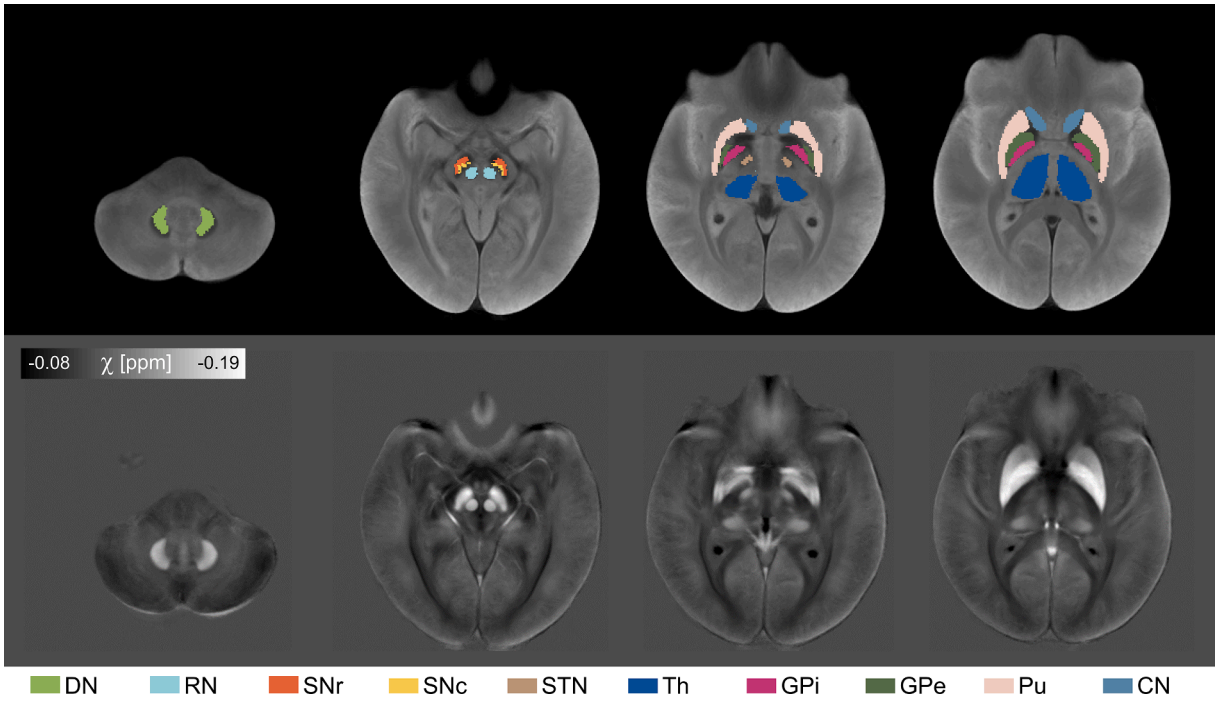

Fig. 2. The top row shows the ROIs used in the QSM analysis overlaid onto the study-specific template, which was computed from the across-TEs average of the T2*-weighted magnitude image of each subject. In the bottom row the corresponding susceptibility maps computed from the first TE averaged over all the subjects in the template space is displayed.

susceptibility maps computed at longer TEs, χ differences between groups were reduced and did not reach statistical significance. Fig. 5 displays the dependence on TE of an exemplary feature, i.e., mean susceptibility, in each ROI for the three groups. While short echo times, such as TE01 and TE02, allowed group discrimination, at longer TEs the measured values for each population were similar: at TE01 and TE02, we reported statistically significant group differences in 11 and 10 ROIs respectively, but only in 4 ROIs at TE03 and 1 at TE04. This finding indicates that the TE-dependence of the histogram features differs in the three populations.

The diagnostic accuracy provided by each histogram feature at each TE was evaluated via ROC analysis. In Fig. 6, the AUC is reported as a measurement of diagnostic accuracy. Generally, the AUC tended to be higher for short TEs (i.e., TE01 and TE02), for which excellent diagnostic accuracy (up to 0.92) was achieved. The mean, the standard deviation, the 75th and the 90th percentile yielded the highest accuracy overall. In the discrimination of MSAp and HC, the 75th percentile of the susceptibility distribution in left GPe at TE02 showed the highest AUC of 0.917, with a specificity of 0.938 and a sensitivity of 0.889. When considering MSAc and HC, the highest AUC of 0.925 was found for the standard

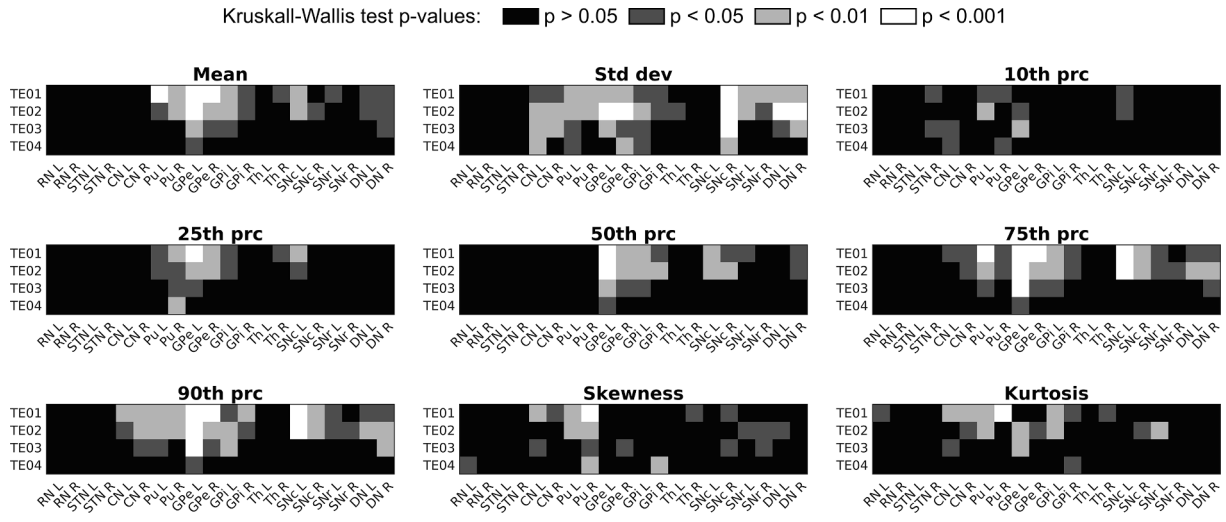

Fig. 3. The gray-level in each plot indicates the p-values obtained by comparing a specific histogram feature of QSM data among the three groups (HC, MSAc and MSAp) via Kruskal-Wallis test for each TE (indicated as TE01, TE02, TE03 and TE04) and each ROI. Overall, the features reaching the highest statistical significance in group discrimination are the mean, the standard deviation, the 75th and the 90th percentile. Smaller p-values are obtained with short TEs which enable to detect statistically significant differences even in ROIs that do not exhibit differences when long TEs are used.

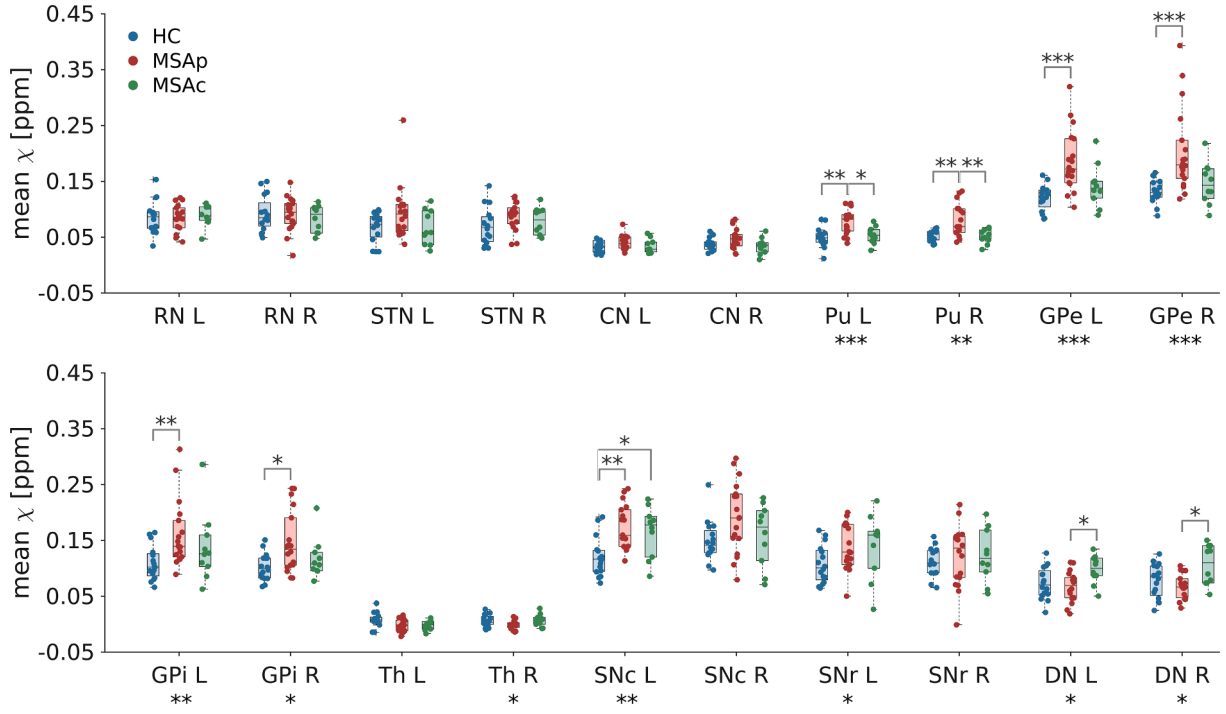

Fig. 4. Each plot shows the sex- and age-adjusted mean QSM values in each ROI for all subjects (HC in blue, MSAp in red and MSAc in green) as scattered dots overlaid on the corresponding boxplot. These values were extracted from maps computed from the first TE (TE01 = 7.38 ms), which shows the highest number of significant alterations. The bottom and top edges of each box indicate the first and the third quartile respectively of the susceptibility distribution across subjects and the central black line indicates the median across subjects in the corresponding group. The level of significance of the Kruskal-Wallis test is reported by the asterisks below the corresponding ROI, while post-hoc Dunn's tests reaching significance after Dunn-Sidak correction for multiple comparison are indicated by the asterisks above the boxplots (* $p < 0.05$, ** $p < 0.01$, *** $p < 0.001$). (For interpretation of the references to colour in this figure legend, the reader is referred to the web version of this article.)

deviation of TE02 in left DN with a specificity of 0.813 and a sensitivity of 0.900. In the classification of the two phenotypes of MSA, the standard deviation of TE02 in right DN yielded the highest AUC of 0.922 with a specificity of 0.944 and a sensitivity of 0.800. Instead, the simple mean-based analysis yielded lower AUC values: specifically, in discriminating MSAp from HC, MSAc from HC, and MSAp from MSAc, the highest AUC were 0.906 (left GPe at TE02), 0.775 (left SNc at TE01) and 0.828 (right Pu at TE01), respectively. The ROC curves computed for these features are shown in Fig. 6.

4. Discussion

In this study we computed susceptibility maps on a population of patients with MSA of both cerebellar and Parkinsonian phenotypes and a population of healthy controls in order to investigate the diagnostic value of QSM. Specifically, we performed an ROI-based analysis

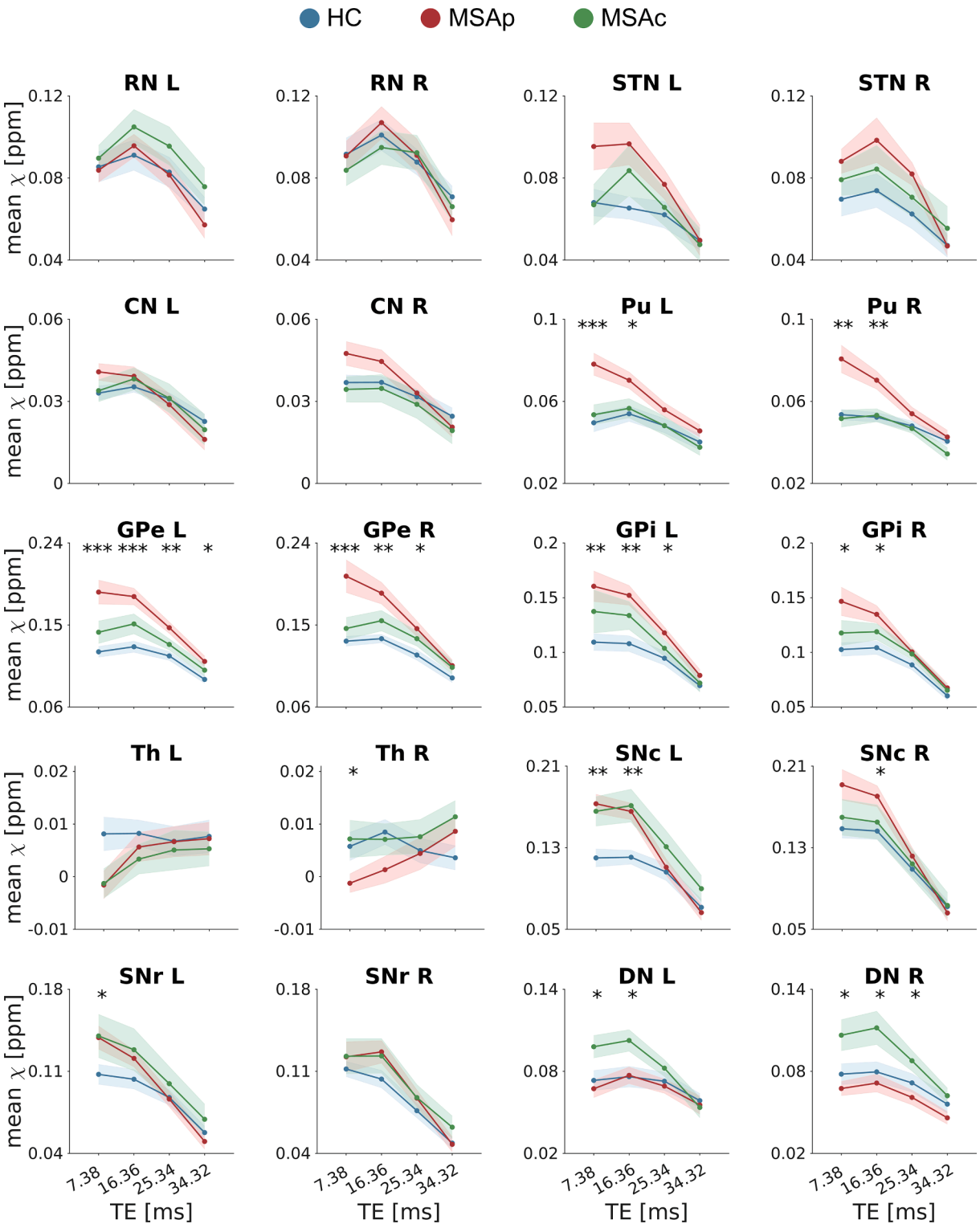

Fig. 5. Dependence on TE of the group differences in mean susceptibility. Each plot displays the mean susceptibility in one ROI for the three groups: HC (blue line), MSAp (red line) and MSAc (green line). The shaded area represents the standard error of the mean, and the asterisks indicate the TEs at which the difference in mean susceptibility across groups reaches significance in the Kruskal-Wallis omnibus test (* $p < 0.05$, ** $p < 0.01$, *** $p < 0.001$). At longer TEs the measured values for each population tends to converge, preventing groups discrimination. (For interpretation of the references to colour in this figure legend, the reader is referred to the web version of this article.)

targeting deep gray matter structures and explored the effect of TE on classification accuracy and the diagnostic potential of a set of histogram features.

We found alterations of the susceptibility distribution in several regions for both phenotypes, including Pu, SN, GP and CN for MSAp and SN and DN for MSAc, highlighting a distributed pattern of iron load alteration. These findings are in agreement with histopathological reports (Dickson et al., 1999; Jellinger, 2003; Matsusue et al., 2009) and previous neuroimaging studies which reported higher susceptibility in Pu and SN for MSAp patients (Sjöström et al., 2017) and in SN and DN

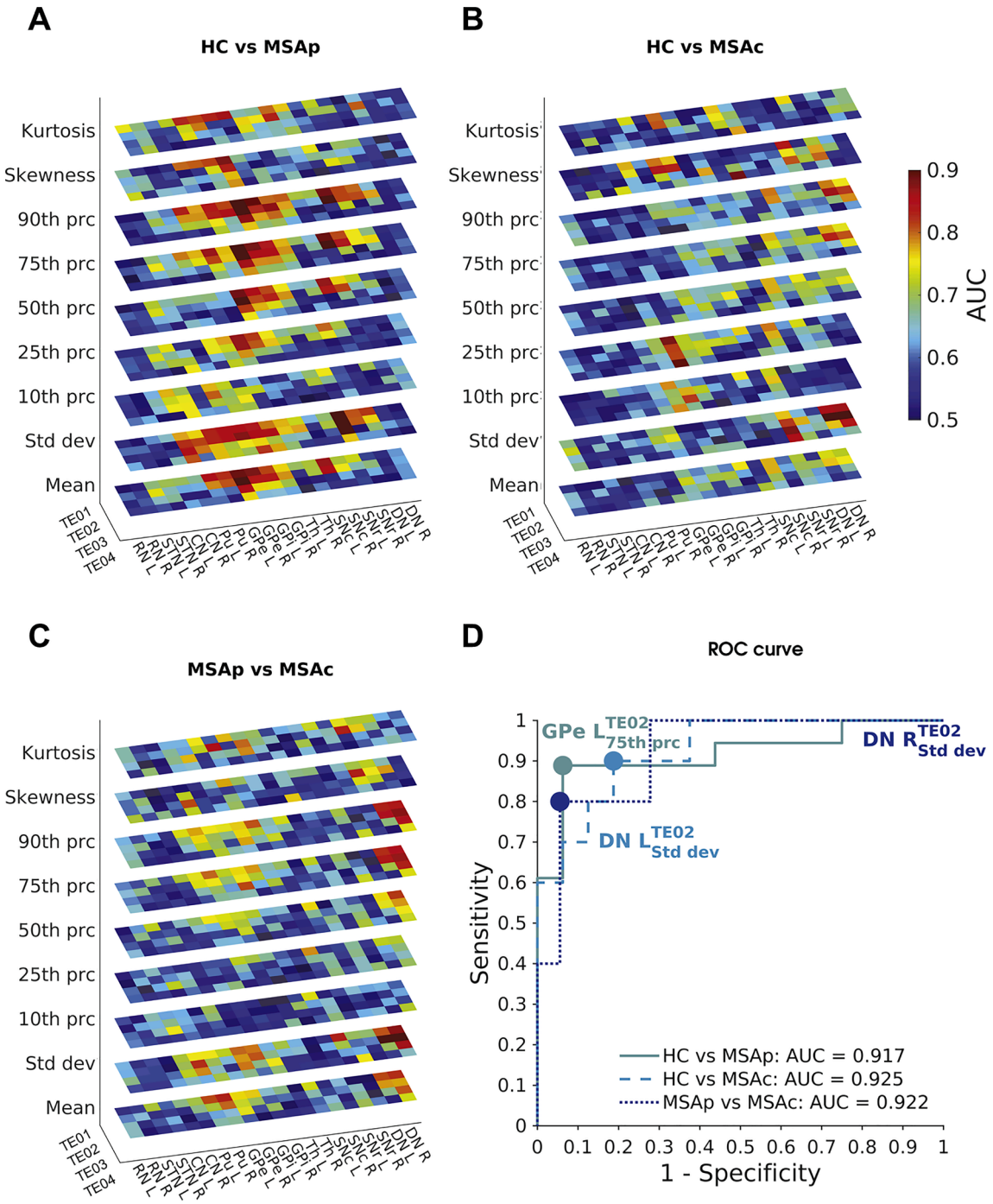

Fig. 6. In panels A-C the diagnostic accuracy for each group pair (HC vs MSAp, HC vs MSAc and MSAp vs MSAc) is displayed. Colors represent the values of the area under the ROC curve (AUC) for each TE, for each ROI and for each histogram feature. It can be noticed that AUC values are higher for short TEs. In panel D, we reported the ROC curve computed for the combinations of TE, ROI and histogram feature yielding the highest AUC for each comparison between groups. The dots represent the optimal cut-off values of each curve.

for MSAc patients (Sugiyama et al., 2019) compared to healthy controls. Interestingly, we observed significantly increased iron deposition in MSA patients in a higher number of ROIs at short echo times, i.e., the first two TEs. These ROIs also included nuclei not previously reported in other QSM studies on MSA, such as GP and CN, but in agreement with post-mortem findings (Dexter et al., 1991; Jellinger, 2003). We attributed this result to the increased sensitivity yielded by short TEs and, especially for CN, histogram features other than the mean.

The dependence of the diagnostic accuracy of QSM on TE is attributable to the non-linear time-evolution of the phase signal. Previous studies observed this phenomenon in several brain tissues, involving both white and gray matter structures, and both cortical and subcortical regions (Cronin et al., 2017; Sood et al., 2017), due to a mechanism involving tissue microstructure and intra-voxel compartmentalization (Sati et al., 2013; Sood et al., 2017; Wharton and Bowtell, 2012; Xu et al., 2018). Modeling the complex gray matter microstructure is remarkably challenging, but, even in white matter, the multi-component simulations of phase evolution could only partially explain the variability of measured susceptibility across TEs (Cronin et al., 2017). Even though QSM provides reproducible measurements of tissue

susceptibility for matching TEs at the same field strength (Lancione et al., 2019; Rua et al., 2020; Spincemaille et al., 2020) when scanning parameters such as coverage (Elkady et al., 2016; Karsa et al., 2018) and spatial resolution (Karsa et al., 2018; Zhou et al., 2017) are fixed and the subject's head is accurately positioned along the same orientation (Cronin and Bowtell, 2018; Lancione et al., 2017; Li et al., 2012), the choice of these experimental factors can affect differently the susceptibility values measured in distinct populations. In fact, the net magnitude and phase signal from a voxel with inhomogeneous composition sampled at a certain TE contain information on the subcompartments whose relaxation time T2* is not much shorter than TE. In the case of MSA, the rapidly-decaying contribution of strong susceptibility sources, such as iron, which is present to a different extent in patients and controls, vanished for long TEs, preventing the detection of differences between the groups. Hence, when designing a clinical protocol involving single-echo QSM, TE should be chosen carefully, depending on the target ROI. Not only its average T2* measured in healthy controls should be taken into account, but also the shorter T2* of sub-voxels compounds that may originate from pathological processes. These values will also depend on the magnetic field strength and on 3T scanners they will be generally longer than the ones presented here at 7T (Lancione et al., 2019). It is worth pointing out that in this work we investigated individual echoes of a multi-echo sequence. While all TEs were acquired with the same bandwidth in our protocol, the results on single-echo acquisitions may differ due to the selection of the optimal bandwidth for the particular TE. On the other hand, each TE of multi-echo QSM sequences may be reconstructed and analyzed independently in order to get an insight into the tissue microstructures. One possible confounding factor in the evaluation of the diagnostic performance concerns the different Signal- and Contrast-to-Noise Ratio (SNR; CNR) of the maps obtained at different TEs. Longer TEs may be less informative due to lower image quality or extreme phase wrapping while short TEs may suffer from low CNR. However, the TEs analyzed in this study are neither extremely long nor short: TE01 = 7.38 ms and TE04 = 34.32 ms are respectively longer and shorter than the first echo usually acquired in multi-echo GRE images at 7T (Rua et al., 2020), while TE03 = 25.34 ms is close to the optimal TE typically used at 7T to maximize the contrast between gray and white matter. Moreover, to rule out the possibility that the variability of diagnostic accuracy is due to higher SNR rather than TE, we repeated the group comparison analysis by using the susceptibility map obtained by averaging all TEs. The results are reported in Supplementary Fig. S3. It can be observed that, despite having higher SNR and CNR than single-echo maps (Denk and Rauscher, 2010), the average QSM shows lower sensitivity in detecting group differences than the first two TEs.

In addition to the mean susceptibility, other histogram features yielded excellent diagnostic accuracy in discriminating patients from controls and between phenotypes, with values of AUC above 0.9. In particular, the standard deviation, the 75^{th} and the 90^{th} percentile were the most informative features. This may reflect the non-uniform alteration of the spatial distribution of iron deposition in some regions, as shown in Supplementary Fig. S4. For example, in patients with MSAp the putamina showed increased susceptibility in their posterolateral portion rather than the anterior part (Ito et al., 2017). This effect may be detected more easily by analyzing histogram features relating to the tails of the distribution, rather than the mean, in agreement with a previous study that reported the highest diagnostic accuracy in differentiating patients with Parkinson's disease from healthy controls for the 10^{th}/75^{th}/90^{th} percentiles and the skewness of the distribution (Zhang et al., 2022). Also, in ROIs presenting inner subdivisions that are difficult to identify especially in patients, such as the trilaminar structure of substantia nigra in Parkinson's disease, histogram analysis performed on the whole-volume of the ROI may help in separating the contributions of different structures (Kim et al., 2018; Li et al., 2019). Future studies should focus on the potential of radiomics second-order textures (Cheng et al., 2019; Li et al., 2019; Xiao et al., 2019) and on the application of advanced multivariate methods based on multivoxel pattern analysis. These approaches may reveal fine-grained textures of iron loads and enhance the classification power of QSM in the early differential diagnosis of neurodegenerative disorders.

The relatively small population included in the current study, due to the low prevalence of MSA, may represent a limitation. However, the high level of statistical significance of the results here reported supports the reliability of findings. A larger cohort of subjects would enable the analysis of subgroups of patients based on the presence or the absence of additional clinical manifestations of interest, as well as the application of machine learning algorithms for feature selection and cross-validation that could improve the diagnostic accuracy by combining the information coming from different features and ROIs (Cheng et al., 2019; Xiao et al., 2019). As definite confirmation of the diagnosis of MSA is obtained via ex-vivo examination, one possible limitation of this study is related to the risk of misdiagnosis, as patients were clinically evaluated without post-mortem pathological confirmation. However, the diagnosis performed at the time of the enrollment in the study was clinically confirmed by neurologists in the follow-up evaluations for all patients. The ROIs employed in this study were selected from published atlases and automatically registered to the study-specific template, in order to avoid subjective biases affecting manual segmentation. Visual inspection by one experienced neuroradiologist excluded the presence of registration errors that could have affected the results of this study. Similarly, the adopted choice of using unreferenced QSM values (which are therefore referred to the average susceptibility in the acquired volume) should not have influenced our results, as the use of reference region provides negligible corrections (Acosta-Cabronero et al., 2016).

In conclusion, we demonstrated that the use of short TEs enhances the diagnostic performance of QSM, improving its capability in detecting altered iron deposition in deep gray matter nuclei. Notably, it allowed the detection of significant susceptibility increase in previously unreported ROIs. Hence, a targeted choice of TE can increase QSM importance in the diagnosis and differential diagnosis of neurodegenerative diseases. Finally, the analysis of histogram features other than the mean may detect subtle differences in the pattern of susceptibility increase, reflecting not just the overall iron accumulation but also heterogeneities in its spatial distribution within a brain region.

Funding

The study was supported by the research program "Bando ricerca finalizzata 2016" of the Italian Ministry of Health (reference number RF-2016-02361597). This study was also partially supported by grant RC and the 5x1000 voluntary contributions, to IRCCS Fondazione Stella Maris, funded by the Italian Ministry of Health. The funding sources had no role in the design and conduct of the study; in the collection, analysis, and interpretation of the data; or in the preparation, review, and approval of the manuscript.

CRediT authorship contribution statement

Marta Lancione: Conceptualization, Methodology, Software, Formal analysis, Investigation, Visualization, Writing – original draft. **Matteo Cencini:** Conceptualization, Methodology, Formal analysis, Investigation, Visualization, Writing – original draft. **Mauro Costagli:** Conceptualization, Methodology, Software, Investigation, Funding acquisition, Writing – review & editing. **Graziella Donatelli:** Conceptualization, Methodology, Investigation, Writing – review & editing. **Michela Tosetti:** Conceptualization, Resources, Project administration, Writing – review & editing. **Giulia Giannini:** Conceptualization, Investigation, Resources, Writing – review & editing. **Roberta Zangaglia:** Conceptualization, Investigation, Resources, Writing – review & editing. **Giovanna Calandra-Buonaura:** Conceptualization, Investigation, Resources, Writing – review & editing. **Claudio Pacchetti:** Conceptualization, Resources, Investigation, Project administration,

Funding acquisition, Writing – review & editing. **Pietro Cortelli:** Conceptualization, Resources, Investigation, Project administration, Funding acquisition, Writing – review & editing. **Mirco Cosottini:** Conceptualization, Resources, Investigation, Project administration, Funding acquisition, Writing – review & editing.

Declaration of Competing Interest

The authors declare the following financial interests/personal relationships which may be considered as potential competing interests: Mirco Cosottini received a speaker honorarium from GE Healthcare. All other authors declare no conflict of interest.

Appendix A. Supplementary data

Supplementary data to this article can be found online at https://doi.org/10.1016/j.nicl.2022.102989.

References

Acosta-Cabronero, J., Betts, M.J., Cardenas-Blanco, A., Yang, S., Nestor, P.J., 2016. In Vivo MRI Mapping of brain iron deposition across the adult lifespan. Neurobiol. Dis. 36, 364–374. https://doi.org/10.1523/JNEUROSCI.1907-15.2016.

Acosta-Cabronero, J., Cardenas-Blanco, A., Betts, M.J., Butryn, M., Valdes-Herrera, J.P., Galazky, I., Nestor, P.J., 2017. The whole-brain pattern of magnetic susceptibility perturbations in Parkinson's disease. Brain 140, 118–131. https://doi.org/10.1093/brain/aww278.

Avants, B.B., Epstein, C.L., Grossman, M., Gee, J.C., 2008. Symmetric diffeomorphic image registration with cross-correlation: Evaluating automated labeling of elderly and neurodegenerative brain. Med. Image Anal. 12, 26–41. https://doi.org/10.1016/j.media.2007.06.004.

Azuma, M., Hirai, T., Nakaura, T., Kitajima, M., Yamashita, S., Hashimoto, M., Yamada, K., Uetani, H., Yamashita, Y., Wang, Y.i., 2019. Combining quantitative susceptibility mapping to the morphometric index in differentiating between progressive supranuclear palsy and Parkinson's disease. J. Neurol. Sci. 406, 116443. https://doi.org/10.1016/j.jns.2019.116443.

Berg, D., Hochstrasser, H., 2006. Iron metabolism in parkinsonian syndromes. Mov. Disord. 21, 1299–1310. https://doi.org/10.1002/mds.21020.

Biondetti, E., Karsa, A., Thomas, D.L., Shmueli, K., 2020. Investigating the accuracy and precision of TE-dependent versus multi-echo QSM using Laplacian-based methods at 3 T. Magn. Reson. Med. 84 (6), 3040–3053. https://doi.org/10.1002/mrm.28331.

Cheng, Z., Zhang, J., He, N., Li, Y., Wen, Y., Xu, H., Tang, R., Jin, Z., Haacke, E.M., Yan, F., Qian, D., 2019. Radiomic Features of the Nigrosome-1 Region of the Substantia Nigra: Using Quantitative Susceptibility Mapping to Assist the Diagnosis of Idiopathic Parkinson's Disease. Front. Aging Neurosci. 11, 167. https://doi.org/10.3389/fnagi.2019.00167.

Cronin, M.J., Bowtell, R., 2018. Quantifying MRI frequency shifts due to structures with anisotropic magnetic susceptibility using pyrolytic graphite sheet. Sci. Rep. 8, 6259. https://doi.org/10.1038/s41598-018-24650-2.

Cronin, M.J., Wang, N., Decker, K.S., Wei, H., Zhu, W.-Z., Liu, C., 2017. Exploring the origins of echo-time-dependent quantitative susceptibility mapping (QSM) measurements in healthy tissue and cerebral microbleeds. Neuroimage 149, 98–113. https://doi.org/10.1016/j.neuroimage.2017.01.053.

de Rochefort, L., Liu, T., Kressler, B., Liu, J., Spincemaille, P., Lebon, V., Wu, J., Wang, Y., 2010. Quantitative susceptibility map reconstruction from MR phase data using bayesian regularization: Validation and application to brain imaging. Magn. Reson. Med. 63, 194–206. https://doi.org/10.1002/mrm.22187.

Deistung, A., Schweser, F., Reichenbach, J.R., 2016. Overview of quantitative susceptibility mapping. NMR Biomed. https://doi.org/10.1002/nbm.3569.

Denk, C., Rauscher, A., 2010. Susceptibility weighted imaging with multiple echoes. J. Magn. Reson. Imaging 31, 185–191. https://doi.org/10.1002/jmri.21995.

Dexter, D.T., Carayon, A., Javoy-agid, F., Agid, Y., Wells, F.R., Daniel, S.E., Lees, A.J., Jenner, P., Marsden, C.D., 1991. Alterations in the levels of iron, ferritin and other trace metals in parkinson's disease and other neurodegenerative diseases affecting the basal ganglia. Brain 114, 1953–1975. https://doi.org/10.1093/brain/114.4.1953.

Dickson, D.W., Lin, W.L., Liu, W.K., Yen, S.H., 1999. Multiple system atrophy: A sporadic synucleinopathy. In: Brain Pathology. International Society of Neuropathology, pp. 721–732. https://doi.org/10.1111/j.1750-3639.1999.tb00553.x.

Düzel, E., Costagli, M., Donatelli, G., Speck, O., Cosottini, M., 2021. Studying Alzheimer disease, Parkinson disease, and amyotrophic lateral sclerosis with 7-T magnetic resonance. Eur. Radiol. Exp. 5 (1) https://doi.org/10.1186/s41747-021-00221-5.

Elkady, A.M., Sun, H., Wilman, A.H., 2016. Importance of extended spatial coverage for quantitative susceptibility mapping of iron-rich deep gray matter. Magn. Reson. Imaging 34, 574–578. https://doi.org/10.1016/J.MRI.2015.12.032.

Fujima, N., Homma, A., Harada, T., Shimizu, Y., Tha, K.K., Kano, S., Mizumachi, T., Li, R., Kudo, K., Shirato, H., 2019. The utility of MRI histogram and texture analysis for the prediction of histological diagnosis in head and neck malignancies. Cancer Imaging 19, 1–10. https://doi.org/10.1186/S40644-019-0193-9/FIGURES/5.

Fujima, N., Kameda, H., Tsukahara, A., Yoshida, D., Sakashita, T., Homma, A., Tha, K.K., Kudo, K., Shirato, H., 2015. Diagnostic value of tumor blood flow and its histogram analysis obtained with pCASL to differentiate sinonasal malignant lymphoma from squamous cell carcinoma. Eur. J. Radiol. 84, 2187–2193. https://doi.org/10.1016/J.EJRAD.2015.07.026.

Gilman, S., Wenning, G.K., Low, P.A., Brooks, D.J., Mathias, C.J., Trojanowski, J.Q., Wood, N.W., Colosimo, C., Dürr, A., Fowler, C.J., Kaufmann, H., Klockgether, T., Lees, A., Poewe, W., Quinn, N., Revesz, T., Robertson, D., Sandroni, P., Seppi, K., Vidailhet, M., 2008. Second consensus statement on the diagnosis of multiple system atrophy. Neurology 71, 670–676. https://doi.org/10.1212/01.wnl.0000324625.00404.15.

Guan, X., Huang, P., Zeng, Q., Liu, C., Wei, H., Xuan, M., Gu, Q., Xu, X., Wang, N., Yu, X., Luo, X., Zhang, M., 2019. Quantitative susceptibility mapping as a biomarker for evaluating white matter alterations in Parkinson's disease. Brain Imaging Behav. 13, 220–231. https://doi.org/10.1007/s11682-018-9842-z.

Haacke, E.M., Liu, S., Buch, S., Zheng, W., Wu, D., Ye, Y., 2015. Quantitative susceptibility mapping: current status and future directions. Magn. Reson. Imaging. 33 (1), 1–25. https://doi.org/10.1016/j.mri.2014.09.004.

He, N., Langley, J., Huddleston, D.E., Ling, H., Xu, H., Liu, C., Yan, F., Hu, X.P., 2017. Improved Neuroimaging Atlas of the Dentate Nucleus. Cerebellum 16, 951–956. https://doi.org/10.1007/s12311-017-0872-7.

Ito, K., Ohtsuka, C., Yoshioka, K., Kameda, H., Yokosawa, S., Sato, R., Terayama, Y., Sasaki, M., 2017. Differential diagnosis of parkinsonism by a combined use of diffusion kurtosis imaging and quantitative susceptibility mapping. Neuroradiology 59, 759–769. https://doi.org/10.1007/s00234-017-1870-7.

Jellinger, K.A., 2003. Neuropathological spectrum of synucleinopathies. Mov. Disord. 18, 2–12. https://doi.org/10.1002/mds.10557.

Karsa, A., Punwani, S., Shmueli, K., Anita Karsa, C., 2018. The effect of low resolution and coverage on the accuracy of susceptibility mapping. Magn. Reson. Med. 1–16 https://doi.org/10.1002/mrm.27542.

Kim, E.Y., Sung, Y.H., Shin, H.G., Noh, Y., Nam, Y., Lee, J., 2018. Diagnosis of early-stage idiopathic parkinson's disease using high-resolution quantitative susceptibility mapping combined with histogram analysis in the substantia nigra at 3 t. J. Clin. Neurol. 14, 90–97. https://doi.org/10.3988/jcn.2018.14.1.90.

Lancione, M., Donatelli, G., Cecchi, P., Cosottini, M., Tosetti, M., Costagli, M., 2019. Echo-time dependency of quantitative susceptibility mapping reproducibility at different magnetic field strengths. Neuroimage 197, 557–564. https://doi.org/10.1016/j.neuroimage.2019.05.004.

Lancione, M., Tosetti, M., Donatelli, G., Cosottini, M., Costagli, M., 2017. The impact of white matter fiber orientation in single-acquisition quantitative susceptibility mapping. NMR Biomed. 30 (11), e3798. https://doi.org/10.1002/nbm.3798.

Langkammer, C., Pirpamer, L., Seiler, S., Deistung, A., Schweser, F., Franthal, S., Homayoon, N., Katschnig-Winter, P., Koegl-Wallner, M., Pendl, T., Stoegerer, E.M., Wenzel, K., Fazekas, F., Ropele, S., Reichenbach, J.R., Schmidt, R., Schwingenschuh, P., 2016. Quantitative susceptibility mapping in parkinson's disease. PLoS One 11, e0162460. https://doi.org/10.1371/journal.pone.0162460.

Langkammer, C., Schweser, F., Krebs, N., Deistung, A., Goessler, W., Scheurer, E., Sommer, K., Reishofer, G., Yen, K., Fazekas, F., Ropele, S., Reichenbach, J.R., 2012. Quantitative susceptibility mapping (QSM) as a means to measure brain iron? A post mortem validation study. Neuroimage 62, 1593–1599. https://doi.org/10.1016/J.NEUROIMAGE.2012.05.049.

Li, G., Zhai, G., Zhao, X., An, H., Spincemaille, P., Gillen, K.M., Ku, Y., Wang, Y., Huang, D., Li, J., 2019. 3D texture analyses within the substantia nigra of Parkinson's disease patients on quantitative susceptibility maps and R2* maps. Neuroimage 188, 465–472. https://doi.org/10.1016/j.neuroimage.2018.12.041.

Li, W., Wang, N., Yu, F., Han, H., Cao, W., Romero, R., Tantiwongkosi, B., Duong, T.Q., Liu, C., 2015. A method for estimating and removing streaking artifacts in quantitative susceptibility mapping. Neuroimage 108, 111–122. https://doi.org/10.1016/j.neuroimage.2014.12.043.

Li, W., Wu, B., Avram, A.V., Liu, C., 2012. Magnetic susceptibility anisotropy of human brain in vivo and its molecular underpinnings. Neuroimage 59, 2088–2097. https://doi.org/10.1016/j.neuroimage.2011.10.038.

Li, W., Wu, B., Liu, C., 2011. Quantitative susceptibility mapping of human brain reflects spatial variation in tissue composition. Neuroimage 55, 1645–1656. https://doi.org/10.1016/j.neuroimage.2010.11.088.

Liu, C., Li, W., Johnson, G.A., Wu, B., 2011. High-field (9.4T) MRI of brain dysmyelination by quantitative mapping of magnetic susceptibility. Neuroimage 56, 930–938. https://doi.org/10.1016/j.neuroimage.2011.02.024.

Liu, C., Li, W., Tong, K.A., Yeom, K.W., Kuzminski, S., 2015. Susceptibility-weighted imaging and quantitative susceptibility mapping in the brain. J. Magn. Reson. Imaging 42 (1), 23–41. https://doi.org/10.1002/jmri.24768.

Lotfipour, A.K., Wharton, S., Schwarz, S.T., Gontu, V., Schäfer, A., Peters, A.M., Bowtell, R.W., Auer, D.P., Gowland, P.A., Bajaj, N.P.S., 2012. High resolution magnetic susceptibility mapping of the substantia nigra in Parkinson's disease. J. Magn. Reson. Imaging 35, 48–55. https://doi.org/10.1002/jmri.22752.

Matsusue, E., Fujii, S., Kanasaki, Y., Kaminou, T., Ohama, E., Ogawa, T., 2009. Cerebellar lesions in multiple system atrophy: Postmortem MR imaging - Pathologic correlations. Am. J. Neuroradiol. 30, 1725–1730. https://doi.org/10.3174/ajnr.A1662.

Mazzucchi, S., Frosini, D., Costagli, M., Del Prete, E., Donatelli, G., Cecchi, P., Migaleddu, G., Bonuccelli, U., Ceravolo, R., Cosottini, M., 2019. Quantitative susceptibility mapping in atypical Parkinsonisms. NeuroImage Clin. 24, 101999. https://doi.org/10.1016/j.nicl.2019.101999.

Pauli, W.M., Nili, A.N., Tyszka, J.M., 2018. Data Descriptor: A high-resolution probabilistic in vivo atlas of human subcortical brain nuclei. Sci. Data 5, 180063. https://doi.org/10.1038/sdata.2018.63.

Ravanfar, P., Loi, S.M., Syeda, W.T., Van Rheenen, T.E., Bush, A.I., Desmond, P., Cropley, V.L., Lane, D.J.R., Opazo, C.M., Moffat, B.A., Velakoulis, D., Pantelis, C., 2021. Systematic Review: Quantitative Susceptibility Mapping (QSM) of Brain Iron Profile in Neurodegenerative Diseases. Front. Neurosci. 15, 618435 https://doi.org/10.3389/fnins.2021.618435.

Reichenbach, J.R., Schweser, F., Serres, B., Deistung, A., 2015. Quantitative Susceptibility Mapping: Concepts and Applications. Clin. Neuroradiol. 25, 225–230. https://doi.org/10.1007/s00062-015-0432-9.

Rua, C., Clarke, W.T., Driver, I.D., Mougin, O., Morgan, A.T., Clare, S., Francis, S., Muir, K.W., Wise, R.G., Carpenter, T.A., Williams, G.B., Rowe, J.B., Bowtell, R., Rodgers, C.T., 2020. Multi-centre, multi-vendor reproducibility of 7T QSM and R2* in the human brain: Results from the UK7T study. Neuroimage 223, 117358. https://doi.org/10.1016/j.neuroimage.2020.117358.

Sati, P., van Gelderen, P., Silva, A.C., Reich, D.S., Merkle, H., de Zwart, J.A., Duyn, J.H., 2013. Micro-compartment specific T2* relaxation in the brain. Neuroimage 77, 268–278. https://doi.org/10.1016/J.NEUROIMAGE.2013.03.005.

Schofield, M.A., Zhu, Y., 2003. Fast phase unwrapping algorithm for interferometric applications. Opt. Lett. 28, 1194–1196. https://doi.org/10.1364/OL.28.001194.

Schweser, F., Deistung, A., Lehr, B.W., Reichenbach, J.R., 2011. Quantitative imaging of intrinsic magnetic tissue properties using MRI signal phase: an approach to in vivo brain iron metabolism? Neuroimage 54, 2789–2807. https://doi.org/10.1016/j.neuroimage.2010.10.070.

Shmueli, K., de Zwart, J.A., van Gelderen, P., Li, T.-Q., Dodd, S.J., Duyn, J.H., 2009. Magnetic susceptibility mapping of brain tissue in vivo using MRI phase data. Magn. Reson. Med. 62, 1510–1522. https://doi.org/10.1002/mrm.22135.

Sjöström, H., Granberg, T., Westman, E., Svenningsson, P., 2017. Quantitative susceptibility mapping differentiates between parkinsonian disorders. Park. Relat. Disord. 44, 51–57. https://doi.org/10.1016/j.parkreldis.2017.08.029.

Smith, S.M., 2002. Fast robust automated brain extraction. Hum. Brain Mapp. 17, 143–155. https://doi.org/10.1002/hbm.10062.

Sood, S., Urriola, J., Reutens, D., O'Brien, K., Bollmann, S., Barth, M., Vegh, V., 2017. Echo time-dependent quantitative susceptibility mapping contains information on tissue properties. Magn. Reson. Med. 77, 1946–1958. https://doi.org/10.1002/mrm.26281.

Spincemaille, P., Anderson, J., Wu, G., Yang, B., Fung, M., Li, K.e., Li, S., Kovanlikaya, I., Gupta, A., Kelley, D., Benhamo, N., Wang, Y.i., 2020. Quantitative Susceptibility Mapping: MRI at 7T versus 3T. J. Neuroimaging jon.12669. 30 (1), 65–75. https://doi.org/10.1111/jon.12669.

Sugiyama, A., Sato, N., Kimura, Y., Fujii, H., Maikusa, N., Shigemoto, Y., Suzuki, F., Morimoto, E., Koide, K., Takahashi, Y., Matsuda, H., Kuwabara, S., 2019. Quantifying iron deposition in the cerebellar subtype of multiple system atrophy and spinocerebellar ataxia type 6 by quantitative susceptibility mapping. J. Neurol. Sci. 407, 116525. https://doi.org/10.1016/j.jns.2019.116525.

Thomas, G.E.C., Zarkali, A., Ryten, M., Shmueli, K., Gil-Martinez, A.L., Leyland, L.-A., Mccolgan, P., Acosta-Cabronero, J., Lees, A.J., Weil, R.S., George, M., Thomas, E.C., 2021. Regional brain iron and gene expression provide insights into neurodegeneration in Parkinson's disease. Brain. https://doi.org/10.1093/brain/awab084.

Wang, E.W., Du, G., Lewis, M.M., Lee, E.Y., De Jesus, S., Kanekar, S., Kong, L., Huang, X., 2019. Multimodal MRI evaluation of parkinsonian limbic pathologies. Neurobiol. Aging 76, 194–200. https://doi.org/10.1016/j.neurobiolaging.2019.01.004.

Wang, Y., Liu, T., 2015. Quantitative susceptibility mapping (QSM): Decoding MRI data for a tissue magnetic biomarker. Magn. Reson. Med. 73, 82–101. https://doi.org/10.1002/mrm.25358.

Wharton, S., Bowtell, R., 2015. Effects of white matter microstructure on phase and susceptibility maps. Magn. Reson. Med. 73, 1258–1269. https://doi.org/10.1002/mrm.25189.

Wharton, S., Bowtell, R., 2012. Fiber orientation-dependent white matter contrast in gradient echo MRI. Proc. Natl. Acad. Sci. U. S. A. 109, 18559–18564. https://doi.org/10.1073/pnas.1211075109.

Xiao, B., He, N., Wang, Q., Cheng, Z., Jiao, Y., Haacke, E.M., Yan, F., Shi, F., 2019. Quantitative susceptibility mapping based hybrid feature extraction for diagnosis of Parkinson's disease. NeuroImage Clin. 24, 102070. https://doi.org/10.1016/j.nicl.2019.102070.

Xiao, Y., Fonov, V., Chakravarty, M.M., Beriault, S., Al Subaie, F., Sadikot, A., Pike, G.B., Bertrand, G., Collins, D.L., 2017. A dataset of multi-contrast population-averaged brain MRI atlases of a Parkinson's disease cohort. Data Br. 12, 370–379. https://doi.org/10.1016/j.dib.2017.04.013.

Xu, T., Foxley, S., Kleinnijenhuis, M., Chen, W.C., Miller, K.L., 2018. The effect of realistic geometries on the susceptibility-weighted MR signal in white matter. Magn. Reson. Med. 79, 489–500. https://doi.org/10.1002/mrm.26689.

Zhang, Y., Yang, M., Wang, F., Chen, Y., Liu, R., Zhang, Z., Jiang, Z., 2022. Histogram Analysis of Quantitative Susceptibility Mapping for the Diagnosis of Parkinson's Disease. Acad. Radiol. 29, S71–S79. https://doi.org/10.1016/j.acra.2020.10.027.

Zhou, D., Cho, J., Zhang, J., Spincemaille, P., Wang, Y., 2017. Susceptibility underestimation in a high-susceptibility phantom: Dependence on imaging resolution, magnitude contrast, and other parameters. Magn. Reson. Med. 78, 1080–1086. https://doi.org/10.1002/mrm.26475.